


Correlated physics in an artificial triangular anti-dot lattice

Z. E. Krix ^{*}, H. D. Scammell, and O. P. Sushkov

School of Physics, University of New South Wales, Sydney 2052, Australia



(Received 29 September 2021; accepted 24 January 2022; published 8 February 2022)

This work considers a two-dimensional artificial triangular anti-dot lattice (TAL): a semiconductor-based artificial crystal hosting Dirac cones, flat bands, and Fermi surface nesting. All such single-particle features have dramatic implications for the emergent correlated phases. This work predominantly focuses on the existence of a robust flat band and enumerates the possible correlated phases that follow. We find that the flat band is generated, in the single-particle theory, when charges align themselves along a kagome lattice with the same period as the TAL. The correlated phases are studied using complementary techniques of expansion in strong and weak Coulomb interactions. Our microscopic modeling shows that for the purpose of generating strongly correlated phases, hole-doped TALs have significant advantages over electron-doped ones.

DOI: [10.1103/PhysRevB.105.075120](https://doi.org/10.1103/PhysRevB.105.075120)

I. INTRODUCTION

Systems hosting flat bands have been a strong focus of recent theoretical and experimental investigations. Moiré superlattice structures such as twisted bilayer graphene [1] and twisted transition metal dichalcogenides [2] as well as kagome metals [3] all host flat bands. Interest in these systems stems from the enhanced effect of Coulomb interactions within the flat band. A striking example of this is the emergence of superconductivity in twisted bilayer graphene [4]. In addition to superconductivity, ferromagnetic and charge density wave phases have been predicted [5]. Particularly relevant and exciting experimental results come from the vanadium family of kagome metals, which have recently been found to host superconducting and charge-density-wave ground states [6–11].

In this work we consider a flat band which can be generated in ordinary semiconductors via periodic electrostatic gating. When the applied potential has hexagonal symmetry and is sufficiently repulsive, a 2D system of electrons or holes will develop a flat band and two pairs of Dirac cones [12–14]. An advantage of this approach to generating a flat band is the ability to tune its bandwidth by varying either the modulation strength or the lattice period (which can be tens to hundreds of nanometers). In what follows we refer to these systems as triangular anti-dot lattices (TALs) and, for concreteness, we consider electrons and holes in GaAs. An experimental realization of the TAL in the weak to moderate modulation regime has been developed and the results are to be published [15]. Excitingly, there has been recent experimental progress in the electron-based TAL [16], which demonstrated key band structure features. However, the effective kagome bands discussed here have not yet been considered, nor the use of holes (instead of electrons). Here we show that the hole band structure (which must account for spin-orbit coupling) has the same features of interest, i.e., a flat band and Dirac points, and we present a numerical technique for computing this.

We have found that the flat band of TALs, in a system with either holes or electrons, can be described by an effective tight-binding model on an emergent kagome lattice. We compute the effective on-site Hubbard energy, U_0 , and hopping parameter, t , and we show that $U_0/t \lesssim 10$ for electrons and $\gtrsim 20$ for holes. Within this effective model we consider a number of correlated phases. Specifically, we consider commensurate and incommensurate charge density waves (CDWs), the Mott insulator phase, Stoner ferromagnetism, and electron-electron driven superconductivity. The effective kagome model has significant consequences for the CDW and Mott phases since this affects the geometry of the CDW patterns and the particle densities at which they occur. We present a set of CDW patterns on the kagome lattice for different filling fractions of the flat band and identify which patterns minimize the Coulomb energy. Using our band structure calculations, we show that a TAL with holes develops a flat band at a much weaker modulation than electrons and has significantly stronger interactions.

The electronic band structure and mapping to a Hubbard model is discussed in Sec. II. Section III covers the hole band structure and compares the electron and hole flat bands. Sections IV and V discuss possible strongly and weakly correlated phases.

II. ELECTRON FLAT BAND AND EFFECTIVE KAGOME MODEL

Within a single-electron model we are able to compute both the energy levels and eigenfunctions of the TAL Hamiltonian $H = \mathbf{p}^2/2m + U(\mathbf{r})$ by numerical diagonalization. The superlattice potential, $U(\mathbf{r})$, represents a triangular anti-dot array,

$$U(\mathbf{r}) = 2W \sum_{i=1}^3 \cos(\mathbf{g}_i \cdot \mathbf{r}),$$

$$\mathbf{g}_1 = \frac{4\pi}{\sqrt{3}a}(0, 1),$$

$$\mathbf{g}_2 = \frac{4\pi}{\sqrt{3}a}(1/2, \sqrt{3}/2),$$
(1)

^{*}z.krix@unsw.edu.au

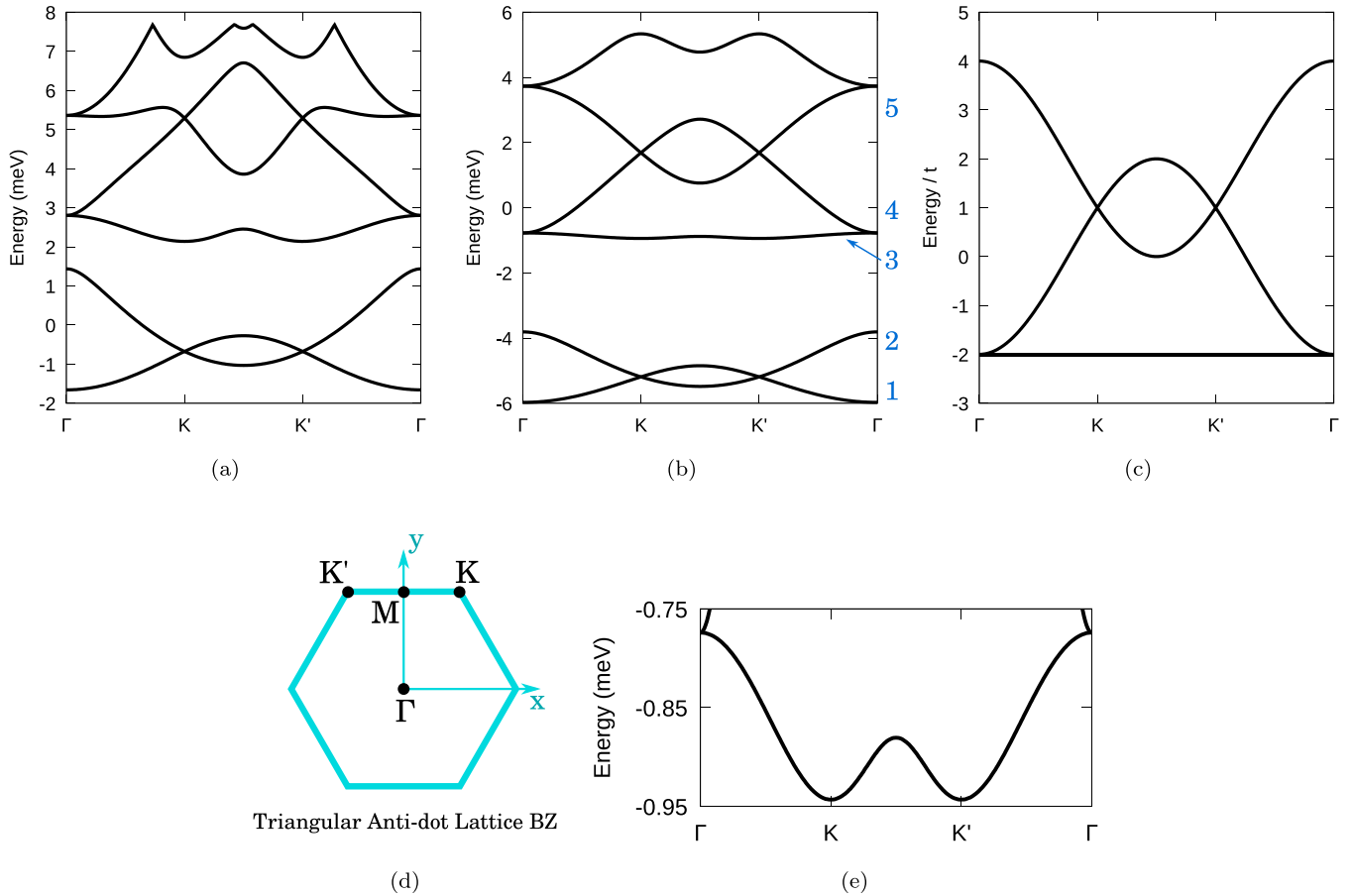


FIG. 1. (a) First six bands of the TAL electronic band structure. The lattice constant is $a = 80$ nm and $W = 1.0E_0$ with $E_0 = 1.57$ meV. Here, Γ is the origin and K and K' are the two nonequivalent Brillouin zone vertices. (b) The same band structure for $W = 2.5E_0$. (c) The three energy bands of the kagome lattice with nearest-neighbor hopping $t > 0$. Band indices are indicated in blue in panel (b). (d) Schematic of the Brillouin zone for the triangular lattice represented by Eq. (1). (e) Close-up of the flat band in panel (b). While there is nonzero band curvature here, it is small compared with the total width of the three kagome-like bands in panel (b).

where $\mathbf{g}_{1,2}$ are the basic vectors of the reciprocal lattice and $\mathbf{g}_3 = \mathbf{g}_2 - \mathbf{g}_1$. The Brillouin zone is shown in Fig. 1(d). For a triangular lattice with lattice spacing a , the reciprocal vectors have length $|\mathbf{g}_i| = 4\pi/\sqrt{3}a$. In Eq. (1), the parameter W controls the strength of the potential. To have an anti-dot array we need this to be positive: $W > 0$ (for $W < 0$ the same potential represents an array of dots). Note that a square-lattice potential is symmetric with respect to the replacement $W \rightarrow -W$. The sinusoidal approximation used in Eq. (1) is justified by the fact that $U(\mathbf{r})$ is generated via electrostatic gating. This means that higher harmonics in the potential, $\mathbf{G} = n\mathbf{g}_1 + m\mathbf{g}_2$ for $|n|, |m| > 1$, are suppressed by a factor $e^{-z|\mathbf{G}|}$, where z is the distance to the gate. For realistic devices, z is sufficiently large and the higher harmonics are negligible.

Numerical diagonalization of H gives both the band structure and the electron wave functions (similar to what was done in Ref. [12]). At a given quasimomentum \mathbf{k} within the Brillouin zone we account for admixture of states with $\mathbf{k}' - \mathbf{k} = m\mathbf{g}_1 + n\mathbf{g}_2$, where m, n are integer numbers. We truncate the Hamiltonian matrix at sufficiently large values of these numbers. The single-particle energy can be expressed in units of $E_0 = \mathbf{K}^2/2m^*$, where m^* is the effective mass of GaAs and $|\mathbf{K}| = 4\pi/3a$ is the momentum at the K point [see Fig. 1(d)]. This scale determines whether a given value of W is

sufficient to strongly reshape the free-particle dispersion. For concreteness, we consider a lattice with $a = 80$ nm in a GaAs quantum well ($E_0 = 1.57$ meV).

At sufficiently large W , the dispersion mimics that of the kagome lattice. The 6 lowest energy bands, calculated with $W = 1.0E_0$ and $W = 2.5E_0$, are shown in Fig. 1 [panels (a) and (b), respectively]. In the same figure, panel (c), we plot the dispersion of a tight-binding model on the kagome lattice with nearest-neighbor, positive hopping parameter t , whose Hamiltonian is

$$H = t \sum_{(i,j)} c_i^\dagger c_j.$$

Here c_i^\dagger is the creation operator for an electron on site i of the kagome lattice. Comparing Figs. 1(b) and 1(c) we conclude that bands 3, 4, and 5 of our TAL reproduce the kagome dispersion very well. Of course, the third band is not perfectly flat [see Fig. 1(e)] but it is close to flat, and, as discussed below, it is even less dispersive for holes. Comparing the total bandwidths of the kagome and TAL dispersions, we can find the effective hopping matrix element t , which is plotted in Fig. 2(a), as a function of the modulation amplitude, W . The typical value of t for electrons is about 0.7 meV.

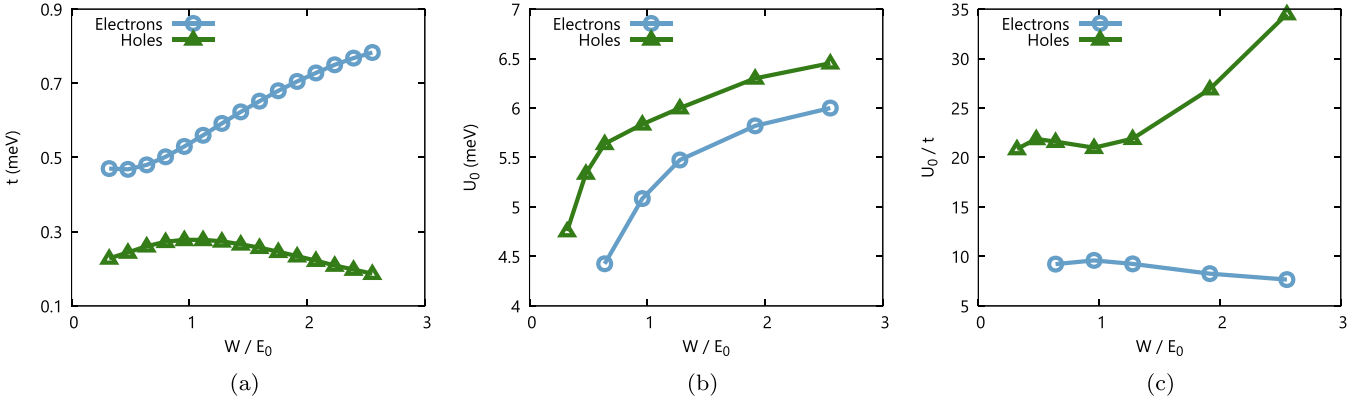


FIG. 2. (a) Effective hopping parameter, t , as a function of the potential strength W . We measure t by equating the total bandwidth of the kagome-like bands [e.g., in Fig. 1(b)] to $6t$, the total band width of Fig. 1(c). Blue corresponds to electrons and green corresponds to holes. (b) Effective Hubbard parameter, U_0 , within the kagome model, as a function of electrostatic potential strength, W . (c) The ratio, U_0/t , between the effective on-site Hubbard repulsion and the effective hopping parameter as a function of W .

Given the Bloch eigenfunctions, $\psi_{m,k}$, of our Hamiltonian, we can calculate the total number density of electrons, $N(\mathbf{r}) = \sum_k |\psi_{m,k}(\mathbf{r})|^2$, for given band, m . The map of the number density corresponding to complete filling of the nearly flat band, $m = 3$, is shown in Fig. 3(a), and the map for complete filling of the kagome-like bands, $m = 3, 4$, and 5, is shown

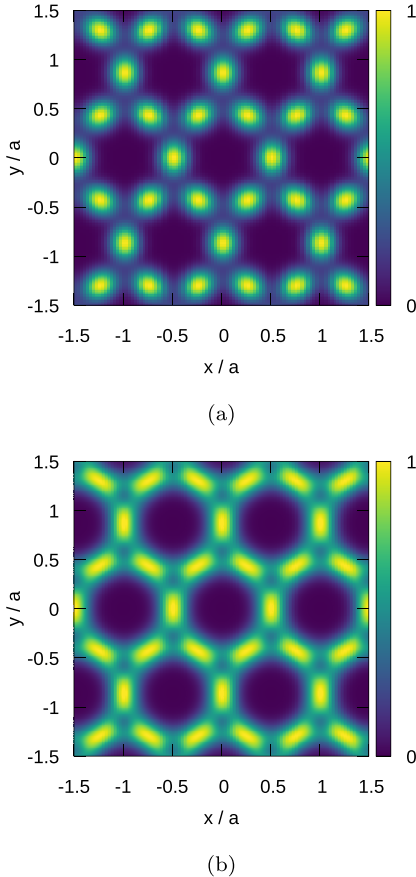


FIG. 3. (a) Charge density of the fully filled flat band in Fig. 1(b). An identical pattern, with reduced intensity, appears for all fractional fillings of the flat band. (b) Total charge density of bands 3, 4, and 5 in Fig. 1(b). In both panels $a = 80$ nm and $W = 2.5E_0$.

in Fig. 3(b). In these maps, the large dark spots (low electron density) are the positions of the anti-dot lattice sites and the bright spots (high electron density) have the symmetry of a kagome lattice. This explains why the triangular anti-dot lattice dispersion emulates that of the kagome model: the kagome-like bands are generated by the formation of an effective kagome lattice within the $m = 3$ energy band.

The bright spots in Fig. 3(a) are well localized and hence a tight-binding approximation is sensible. Within this approximation, we account for the Coulomb interaction between electrons by calculating the on-site Hubbard repulsion U_0 for a given kagome lattice site. The calculation of U_0 proceeds by first treating the electron density profile within a single bright spot as the density $n(\mathbf{r})$ for a single, localized electron. This means that the total band density $N(\mathbf{r})$ is a sum over individual, localized functions $n(\mathbf{r})$. We found that $n(\mathbf{r})$ is well represented by a Gaussian function and we use this fitting in all calculations. Since it corresponds to the charge density of a single electron it must be normalized to unity:

$$\int n(\mathbf{r})d^2r = 1,$$

where, because of the Gaussian fitting, we can take the limits of this integral to be infinite. We can then compute U_0 as

$$U_0 = \frac{e^2}{\epsilon} \int d^2r_1 d^2r_2 \frac{n(\mathbf{r}_1)n(\mathbf{r}_2)}{|\mathbf{r}_1 - \mathbf{r}_2|}.$$

Here, ϵ is the dielectric constant. This integral can be computed analytically in terms of the fitting parameters of the Gaussian $n(\mathbf{r})$. The plot of U_0 as a function modulation amplitude W is presented in Fig. 2(b). Our data correspond to GaAs, for which $\epsilon = 12$ (as in all other calculations, $a = 80$ nm). We find a value for U_0 of around 5–6 meV. In comparison to t , we find that U_0/t is less than around 10 [see Fig. 2(c)]. Thus, the bands $m = 3, 4, 5$ are mapped to the kagome-lattice Hubbard model with Hamiltonian

$$H = t \sum_{(i,j)} c_i^\dagger c_j + U_0 \sum_i n_{i,\uparrow} n_{i,\downarrow}.$$

We find that the parameter U_0 scales with the lattice constant a as $U_0 \sim 1/\sqrt{a}$ at constant W . Since the kinetic energy, t ,

scales as $t \sim 1/a^2$, the ratio U_0/t has the following scaling property:

$$U_0/t \sim a^{3/2}.$$

To complete the analysis of the single-electron model we reiterate that the third band of the anti-dot lattice is nearly flat, but, unlike the pure kagome model, it is not perfectly flat. An enlarged plot of the third band of Fig. 1(b) is given in Fig. 1(e). The minima of this band are at the K points of the Brillouin zone [Fig. 1(d)]. Therefore, at low filling of the flat band, the Fermi surface consists of two electron pockets centered at \mathbf{K} and \mathbf{K}' . The band dispersion near these points is quadratic, $E = \mathbf{q}^2/2m^*$, with an effective mass, m^* [a complete discussion is left to the following section with m^* versus W plotted in Fig. 7(a)].

III. HOLE BAND STRUCTURE AND COMPARISON WITH ELECTRONS

The effective kagome model applies to both holes and electrons; however, the hole superlattice has some significant advantages when it comes to experimental realizations. In this section we demonstrate, using band structure calculations, that holes in a TAL require a much weaker modulation to achieve the same flat band width and interaction strength as electrons.

A. Technique for computing hole band structure

In GaAs the conduction band (relevant to electrons) originates from atomic s orbitals while the valence band (relevant to holes) originates from atomic p orbitals. The valence p band has a significant spin-orbit interaction and hence it is split into a $p_{3/2}$ subband and a $p_{1/2}$ subband. Here, $J = l + s = 1/2$, $3/2$ plays the role of effective spin for each subband. Due to spin-orbit splitting the $p_{1/2}$ subband lies 500 meV below the $p_{3/2}$ subband and therefore $p_{1/2}$ is irrelevant to the low-energy physics considered here. The relevant $p_{3/2}$ subband corresponds to holes that carry an effective spin of $3/2$ and is described by the effective Luttinger Hamiltonian [17] H_L . The total Hamiltonian is

$$H = H_L + w(z) + U(x, y), \quad (2)$$

where $w(z)$ is a confining potential oriented perpendicular to the plane of the artificial lattice [again, defined by $U(x, y)$ from Eq. (1)]. Specifically, $w(z)$ is taken to be an infinite square well of width $d = 15$ nm. The Luttinger Hamiltonian can be written as (Eq. (6) in Ref. [18])

$$\begin{aligned} H_L &= H_0 + V, \\ H_0 &= \left(\gamma_1 + \frac{5}{2}\bar{\gamma} - 2\bar{\gamma}S_z^2 \right) \frac{p_{\perp}^2}{2m_e} + \left(\gamma_1 - \frac{5}{4}\bar{\gamma} + \bar{\gamma}S_z^2 \right) \frac{p_{\parallel}^2}{2m_e}, \\ V &= \frac{-\bar{\gamma}}{4m_e} [p_+^2 S_-^2 + p_-^2 S_+^2 \\ &\quad + 2p_z p_+ \{S_z, S_-\} + 2p_z p_- \{S_z, S_+\}], \end{aligned} \quad (3)$$

where $p_{\pm} \equiv p_x \pm ip_y$ and S_i are the 4×4 spin matrices for a spin $3/2$ particle. For simplicity we used the spherical approximation, $\gamma_2 \approx \gamma_3$, with $\bar{\gamma} \equiv (2\gamma_2 + 3\gamma_3)/5$. The parameters γ_1 and $\bar{\gamma}$ are taken to be 6.85 and 2.58 respectively, values

corresponding to GaAs. Our approach to solving this problem begins with defining an orthonormal set of basis wave functions $\Psi_{k,n,\sigma}$:

$$\Psi_{k,n,\sigma}(\mathbf{r}) = \phi_n(z)\psi_k(x, y)\chi_{\sigma}, \quad (4)$$

where $\phi_n(z)$ is an eigenfunction of the square well, $\psi_k(x, y)$ is a plane wave (eigenfunction of the momentum operator), and χ_{σ} is a spin- $3/2$ spinor (eigenfunction of S_z). As an example, for $\sigma = +3/2$ and arbitrary $n = \text{odd}$ and k ,

$$\Psi_{k,n,\sigma=3/2}(\mathbf{r}) = \sqrt{\frac{2}{d}} \cos(n\pi z/d) \frac{1}{\sqrt{A}} e^{i\mathbf{k}\cdot\mathbf{r}_{\parallel}} \begin{bmatrix} 1 \\ 0 \\ 0 \\ 0 \end{bmatrix}.$$

Here, A is the area of the sample and when n is even \cos changes to \sin . The wave function is also zero for $|z| > d/2$ [i.e., in the region forbidden by $w(z)$]. We can now compute the matrix elements of the Hamiltonian [Eq. (2)] in the basis defined by these functions,

$$H_{k_i, n, \sigma | k_j, m, \tau} = \langle \mathbf{k}_i, n, \sigma | H | \mathbf{k}_j, m, \tau \rangle.$$

With regards to x and y dependence, the nonmodulated part of the Hamiltonian [in Eq. (2)], $H_L + w(z)$, contains only p_x , p_y and has no explicit dependence on the variables x , y . It follows that this part of H is diagonal in the index k_i since the basis vector Ψ is a plane wave in the x - y plane with wave vector \mathbf{k}_i . As for the modulated part of the Hamiltonian, it is well known that a periodic potential, $U(x, y)$, has nonzero matrix elements only between plane waves which differ in momentum by a reciprocal lattice vector. We can thus define a quasimomentum \mathbf{k} and let $\mathbf{k}_i = \mathbf{k} + \mathbf{G}_i$ where \mathbf{G}_i is a reciprocal lattice vector. The matrix elements of the Hamiltonian can then be written as

$$H_{j, m, \tau}^{i, n, \sigma}(\mathbf{k}) = \langle \mathbf{k} + \mathbf{G}_i, n, \sigma | H | \mathbf{k} + \mathbf{G}_j, m, \tau \rangle. \quad (5)$$

We are now in a position to compute these matrix elements explicitly. The expression for H_0 in Eq. (3) contains only S_z , p_z^2 and p_x , p_y . Our basis vectors [Eq. (4)] are, by design, eigenvectors of $H_0 + w(z)$. This part of the Hamiltonian is thus diagonal in all indices i , n , and σ ; its matrix elements are given by H_0 in Eq. (3) with $p_{\parallel} = \mathbf{k} + \mathbf{G}_i$, $p_z^2 = (n\pi/d)^2$, and $S_z = \sigma$. Thus,

$$\begin{aligned} [H_0 + w(z)]_{j, m, \tau}^{i, n, \sigma} &= \delta_{i,j} \delta_{n,m} \delta_{\sigma,\tau} \left[\left(\gamma_1 + \frac{5}{2}\bar{\gamma} - 2\bar{\gamma}\sigma^2 \right) \frac{(n\pi/d)^2}{2m_e} \right. \\ &\quad \left. + \left(\gamma_1 - \frac{5}{4}\bar{\gamma} + \bar{\gamma}\sigma^2 \right) \frac{(\mathbf{k} + \mathbf{G}_i)^2}{2m_e} \right]. \end{aligned}$$

The periodic potential $U(x, y)$ has matrix elements

$$(U)_{j, m, \tau}^{i, n, \sigma} = W \sum_{\alpha=1}^3 \delta(\mathbf{G}_j - \mathbf{G}_i \pm \mathbf{g}_{\alpha}) \delta_{n,m} \delta_{\sigma,\tau}.$$

Lastly, the operator V in Eq. (3) contains p_x and p_y which are diagonal in the indices i , j and will thus be replaced by $\delta_{i,j}(\mathbf{k} + \mathbf{G}_i)_{x,y}$. It also contains $S_{x,y,z}$, whose matrix elements in the indices σ , τ are given, for example, in Ref. [19]. The

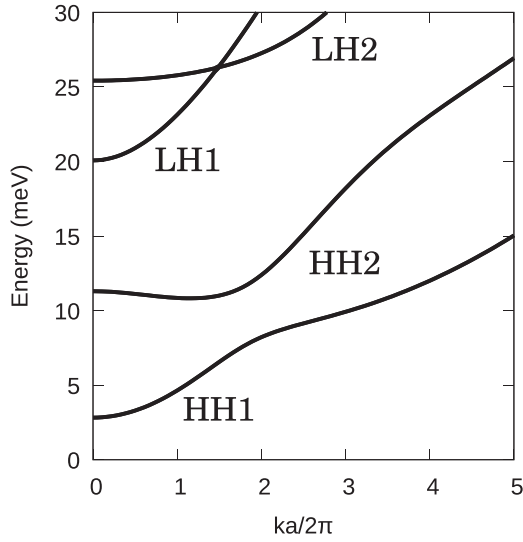


FIG. 4. Bare dispersion for 2D holes in GaAs with an infinite square confining potential. Here, $d = 15$ nm and we measure momentum in units of $2\pi/a$ for $a = 80$ nm (the standard lattice constant throughout this work). This dispersion is isotropic.

only remaining term is p_z , which has matrix elements

$$(p_z)_{i,n,\sigma}^{j,m,\tau} = \delta_{i,j} \delta_{\sigma,\tau} \begin{cases} 0, & n = m, \\ -\frac{2mi}{d} \left[\frac{\sin[(n-m)\pi/2]}{(n-m)} + \frac{\sin[(n+m)\pi/2]}{(n+m)} \right], & \begin{matrix} n = \text{odd}, \\ m = \text{even}, \end{matrix} \\ +\frac{2mi}{d} \left[\frac{\sin[(n-m)\pi/2]}{(n-m)} - \frac{\sin[(n+m)\pi/2]}{(n+m)} \right], & \begin{matrix} n = \text{even}, \\ m = \text{odd}. \end{matrix} \end{cases}$$

The complete matrix for V is then

$$(V)_{i,n,\sigma}^{j,m,\tau} = \frac{-\tilde{\gamma}}{4m_e} \delta_{i,j} [(k + G_i)_+^2 (S_-^2)_{\sigma,\tau} + (k + G_i)_-^2 (S_+^2)_{\sigma,\tau} + 2(p_z)_{n,m} (k + G_i)_+ \{S_z, S_-\}_{\sigma,\tau} + 2(p_z)_{n,m} (k + G_i)_- \{S_z, S_+\}_{\sigma,\tau}].$$

We now have an explicit expression for all the matrix elements of $H = H_0 + w(z) + V + U(x, y)$ in the basis defined by Eq. (4). Energy levels and eigenvectors of H can then be determined by numerical diagonalization, provided we truncate the basis. The truncation procedure amounts to choosing

a maximum value for n and a finite set of reciprocal lattice vectors, \mathbf{G}_i , to include in the basis. To determine appropriate values, we increased the size of the basis until all energy levels of interest converged. The energy levels in the absence of any periodic modulation (shown in Fig. 4), computed using this method, agree with previous calculations [18,20].

B. Hole band structure results

Examples of the hole minibands are presented in Fig. 5. In these calculations the strength of the spin-orbit interaction is governed by the ratio d/a between the well width, d , and the lattice constant, a . We have considered the weak to moderate spin-orbit regime in this work, with $d/a \approx 0.2$. The hole dispersion has a similar form to that of an equivalent electron system, the two lowest energy bands are Dirac-like, and the next three bands are kagome-like [see Fig. 5(c), for example]. There are some key differences, however. Holes in an unmodulated device have a nonparabolic dispersion (Fig. 4) and, in general, will have a different effective mass than electrons. Because of this, the effective mass for holes is a function of momentum and does not have a single, well-defined value. Roughly speaking, however, the unmodulated effective mass for holes is three times larger than that for electrons. The second key difference is the spin-orbit interaction. As mentioned above, holes in GaAs have a non-negligible spin-orbit interaction. The presence of this interaction introduces gaps at the Dirac points and at the flat band that do not exist in the electron band structure. Note that for larger values of d/a this causes a much more significant reshaping of the energy bands (Fig. 6). For example, at $d/a = 0.5$ and $W = 0.5E_0$ the kagome-like bands disappear and the graphene-like bands remain with a large gap relative to the total bandwidth [Fig. 6(b)]. This regime is interesting in connection with artificial topological insulators [21,22], but is not the main focus of this work.

Our central finding with regard to the hole band structure is that the kagome-like bands, including the flat band, develop at a much weaker modulation than for electrons. For example, compare Fig. 1(a) for electrons at $W = E_0$ and Fig. 5(c) for holes at the same W . The hole bands have a well-formed kagome-like dispersion while the electron bands do not. There is also a factor 7 difference in the bandwidth of the third band between holes and electrons, with holes having the much flatter band. The degree of band flatness is captured by the

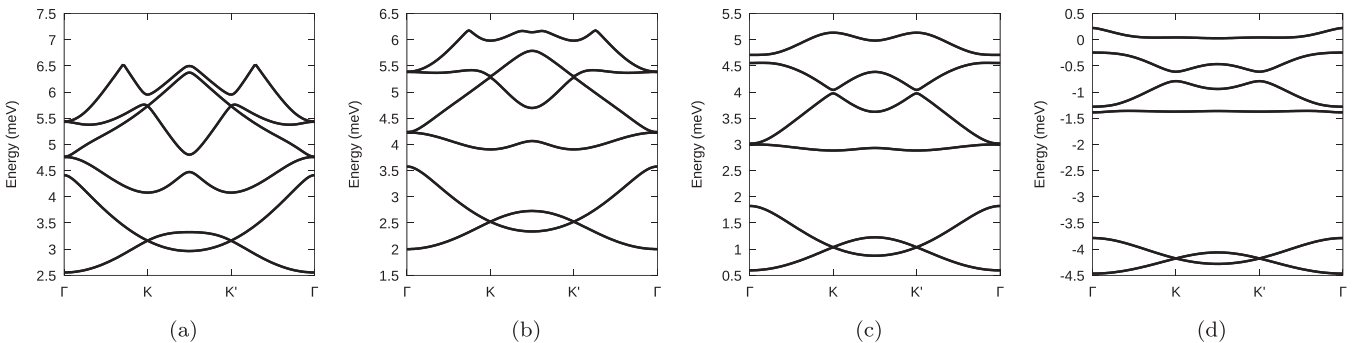


FIG. 5. Energy bands for holes, derived from the Hamiltonian in Eq. (2), for various values of W at $a = 80$ nm and quantum well width $d = 15$ nm. Each hole band is doubly degenerate. (a) $W = 0.25E_0$, (b) $W = 0.50E_0$, (c) $W = 1.00E_0$, (d) $W = 2.50E_0$.

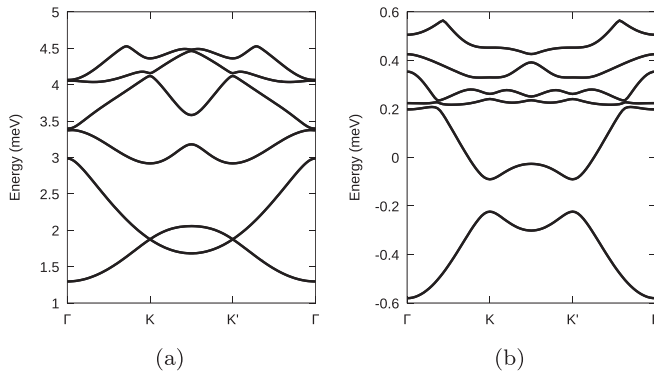


FIG. 6. Lowest 6 bands of the hole band structure for $d = 20$ nm (a) and $d = 40$ nm (b). In both panels $W = 0.5E_0$ and $a = 80$ nm. In panel (b) the gap between the two lowest bands is 14% of the total width of those bands.

curvature around the minimum of the flat band [see Fig. 1(e)]. Since this part of the dispersion is parabolic we can describe it by an effective mass, $\varepsilon(k) = k^2/2m^*$. We compare this effective mass for holes and electrons in Fig. 7(a), from which it can be seen that m^* is 4 to 10 times larger in the hole flat band than in the electron flat band. Figure 7(a) also shows that the effective mass $m^* = 0.2m_e$, for example, is reached at $W \approx 2.5E_0$ for electrons and $W \approx 0.6E_0$ for holes. The third hole band is not just flatter in absolute units; it is also flatter relative to the total width of the kagome-like bands [proportional to t ; Fig. 2(a)]. From Fig. 2(a) it can be seen that t is 2 to 9 times smaller for holes. This decrease in total bandwidth is compensated by a greater decrease in the width of the flat band.

To conclude this section we note that one of the experimental challenges in producing artificial superlattices is generating a strong periodic modulation, sufficient to significantly restructure the energy bands of the 2D system. Our calculations show that hole systems require a much smaller modulation strength to induce flat bands, and hence access strongly correlated phases, than equivalent electron systems.

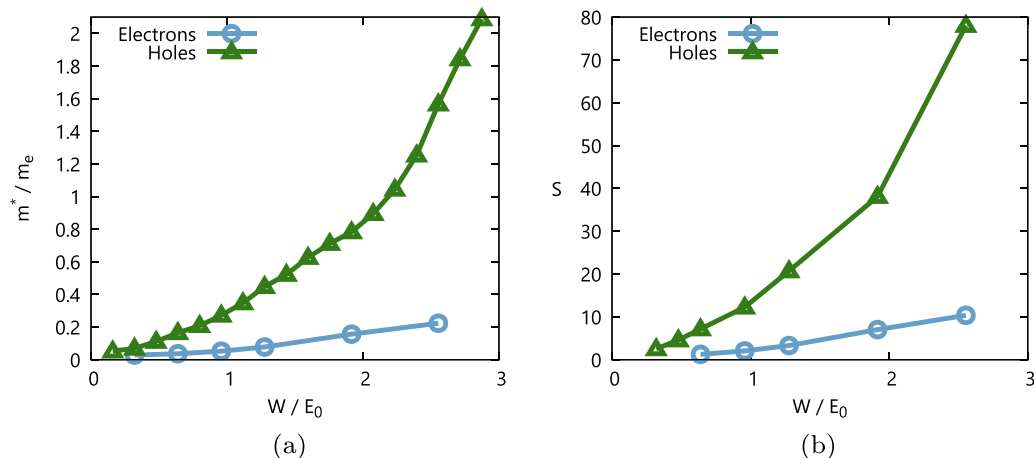


FIG. 7. (a) Effective mass of the flat band [defined around the K points in Fig. 1(e)] as a function of potential strength W for electrons and holes. The quantity $1/m^*$ is roughly proportional to the width of the flat band. (b) Plot of the Stoner parameter, S [Eq. (6)], as a function of W for both electrons and holes.

This is the central conclusion of our hole band structure calculation.

IV. POSSIBLE STRONGLY CORRELATED PHASES WITHIN THE EFFECTIVE KAGOME MODEL

In the present section we discuss some of the possible strongly correlated phases which could arise in TALs. Here we use a strong Coulomb coupling expansion; i.e., the emergent correlated phases are those that minimize the Coulomb energy. In this and the following section we consider only the most anticipated correlated phases. The possibility of other phases such a nematic phase or Pomeranchuk instability could be an interesting avenue of future research.

A. Commensurate charge density waves

The existence of an underlying kagome lattice and the large value of U_0/t [Fig. 2(c)] imply that the on-site localization of electrons (or holes) is highly likely. This localization eliminates on-site Coulomb repulsion; however, longer-range Coulomb repulsion is still present. For example, the distance between nearest kagome sites is $a/2 = 40$ nm. The nearest-site Coulomb repulsion is then very significant,

$$V = \frac{e^2}{\epsilon a/2} \approx 2.7 \text{ meV}.$$

This longer-range Coulomb repulsion can lead to ordering of the localized electrons (or holes). Thus, in this subsection, we consider the corresponding possible commensurate CDWs.

These CDWs would exist on the kagome lattice at certain filling fractions of the kagome-like bands in Fig. 1(b) [or Fig. 5(c)], each filling fraction having a set of possible CDW patterns. Here we consider, for the purposes of illustration, the filling fractions $n = 1n_0$, $(3/2)n_0$, $(4/3)n_0$, and $2n_0$ measured relative to complete filling of the lowest two bands and in units of $n_0 = 1/A_{\text{cell}}$. Thus $n = 1n_0$ corresponds to half filling of the flat band and $n = 2n_0$ corresponds to full filling of the flat band.

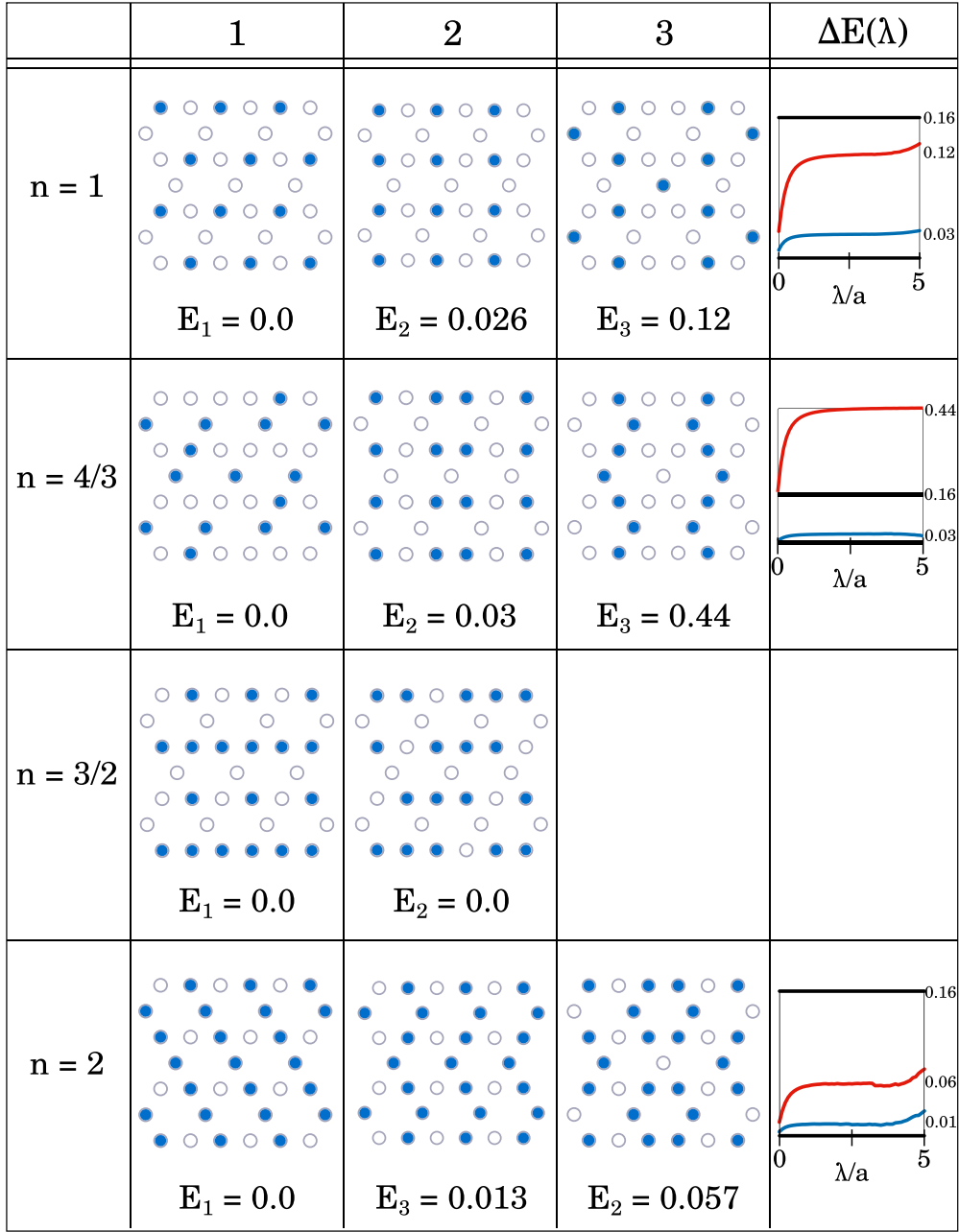


FIG. 8. Summary of results for the average energy per electron of each CDW pattern. Electron density, n , is given in units of one electron per unit cell. Each energy, E_i , was computed for the corresponding pattern pictured in each cell and the patterns are numbered in order of increasing energy. Energy is given in meV measured relative to the lowest energy configuration. The rightmost column plots the energy of each pattern as a function of λ (the screening length) relative to the lowest energy configuration E_1 . A typical flat band width for electrons (0.16 meV) is shown in black and λ varies from 0 to $5a$.

We can now catalog the set of CDW phases that are possible within the flat band. For each filling fraction we found periodic patterns of occupied kagome-lattice sites which give the correct amount of charge per unit cell. These are presented in Fig. 8. There can, in general, be more than one pattern at each filling fraction. For each of these patterns, the Coulomb energy per electron is

$$E = \frac{1}{2N_{\text{sites}}} \sum_{\substack{i,j=1 \\ j \neq i}}^{N_{\text{sites}}} \frac{e^2}{\epsilon r_{ij}} e^{-r_{ij}/\lambda},$$

where i and j represent occupied sites in the CDW, r_{ij} is the distance between sites, and $\lambda \approx 3a$ is the screening length¹ (due to screening by image charges in the metallic gate). There is also $N_{\text{sites}} \rightarrow \infty$, which is the number of occupied lattice sites. To avoid the infinite summation, we define a smaller set of M occupied sites. This block has to be defined such that

¹We find (see the right column of Fig. 8) that the lattice energy is independent of λ for the range $\lambda \in [0.5a, 4a]$. Our quoted value of $\lambda = 3a$ is simply a value within this range.

it can be repeated, periodically, to reconstruct the full CDW pattern. The energy we compute is

$$E = \frac{1}{2M} \sum_{\substack{i=1,M \\ j \neq i}} \frac{e^2}{\epsilon r_{ij}} e^{-r_{ij}/\lambda}.$$

The right column of Fig. 8 shows this energy as a function of λ measured relative to the lowest energy configuration. We find that different CDW patterns at the same density can be distinguished by energies which differ on the order of the electron flat band width and the first column of Fig. 8 identifies the pattern with minimal energy. Since the CDW phase is insulating, its signature in transport measurements will be a maximal value of R_{xx} when particle density is tuned to one of the values given in Fig. 8. If we measure the particle density from the bottom of the lowest energy band then these values are $n_{\text{tot}} = 9 \times 10^{10} \text{ cm}^{-2}$, $9.6 \times 10^{10} \text{ cm}^{-2}$, $9.9 \times 10^{10} \text{ cm}^{-2}$, and $10.8 \times 10^{10} \text{ cm}^{-2}$. Our analysis here has been simplified by ignoring fluctuation effects. Of course, fluctuations could be important in the strongly correlated states; however we believe that they cannot destroy the order.

B. Mott insulator

The Mott insulating phase is related to the CDW phase but occurs exactly at half filling of the kagome lattice (i.e., one particle on each kagome lattice site, $n = 3n_0$). This does not occur within the flat band but within the band directly above it, i.e., at half filling of the second kagome-like band [Figs. 1(b) and 5(c)]. The experimental signature for this phase is the same as for charge density waves except the density at which this occurs is $n_{\text{tot}} = 12.6 \times 10^{10} \text{ cm}^{-2}$. The effective antiferromagnetic exchange between nearest sites in the Mott insulator is $J = 4t^2/U_0 \sim 0.1 \text{ meV}$.

V. POSSIBLE WEAK-COUPPLING PHASES

In this section we continue to analyze possible quantum phases within the flat band [see Fig. 5(a)] using the itinerant picture. We thus account for the Coulomb interaction perturbatively.

The weak Coulomb coupling regime is reached by considering a weak potential modulation, characterized by W/E_0 . For example, in the hole gas, $W/E_0 \lesssim 0.25$ corresponds to weak Coulomb coupling in the kagome flat band. We see from Fig. 5(a) that for $W/E_0 = 0.25$, the flat band shows significant dispersion, whereas for $W/E_0 = 1$, this band is nearly dispersionless.

A. Ferromagnetism

We have pointed out above that because of the large value of U_0/t the localization of electrons/holes is likely. Nevertheless it is instructive to consider the itinerant picture as well. This analysis is probably more relevant to the relatively weak superlattice modulation, $W/E_0 \lesssim 1$.

The flat band together with the second Dirac point [e.g., Fig. 1(b)] is relevant to the effective kagome model but we can also consider the flat band in isolation. In TALs the flat

band still has some small dispersion. As mentioned above, the two minima of the flat band are approximately quadratic [Fig. 1(e)] and we can assign to them an effective mass m^* [Fig. 7(a)]. If we suppose that the chemical potential is within the quadratic part of the flat band (which amounts to roughly less than one-third filling of that band) then we can ask whether the Stoner criterion for ferromagnetism [23] is satisfied. In our system the Stoner criterion can be written as

$$S \equiv \frac{A_{\text{cell}}}{3} U_0 |\Pi_0| > 1, \quad (6)$$

where Π_0 is the 2D polarization operator, which contains a factor 2 due there being two minima in the flat band, at the \mathbf{K}, \mathbf{K}' points. The factor $A_{\text{cell}}/3$ is required by the normalization of our wave functions. To normalize the wave functions we need to obtain unity after summation over the *three* sublattices of the kagome lattice and this introduces a factor $1/3$ to the normalization coefficient. In two dimensions the polarization operator is

$$\Pi_0 = -\frac{m^*}{\pi \hbar^2}.$$

We have plotted $m^*(W)$ and $S(W)$ in Fig. 7. Within both the electron and hole flat bands the Stoner parameter, S , takes values larger than 1, indicating that the lower part of the flat band is well within the Stoner regime. Such large values follow from S being proportional to the density of states, which diverges within the flat band. In connection to this point, the significant difference in S between holes and electrons is due to the hole flat band width being several times smaller.

The presence of a ferromagnetic phase in a 2D material can be determined via observation of an anomalous Hall resistivity. The anomalous Hall effect is exhibited in systems with spin-orbit coupling and manifests as a hysteresis in R_{xy} , measured for up and down sweeps of an external magnetic field (see, for example, Ref. [24]). Since this effect relies on spin-orbit coupling it is only observable for holes and not electrons.

B. Incommensurate spin density wave

Suppose we tune the system below the ferromagnetic Stoner instability, $S < 1$, such that there is no ferromagnetism. This is achieved by lowering W/E_0 . At $W = 0.25E_0$ [Fig. 5(a)], for example, we find that a single ‘‘antiparticle’’ Fermi surface is formed which centers around Γ when the chemical potential is near the top of the third energy band (i.e., the flat band). We find that there exists a critical chemical potential, $\mu = \mu_c$, such that the Fermi surface exhibits nesting, with nesting vectors \mathbf{Q}_i . This Fermi surface and the nesting vectors are shown in Fig. 9(a). A nested Fermi surface with nesting vector \mathbf{Q} typically promotes spin and/or charge density wave (SDW/CDW) ordering with wave vector \mathbf{Q} , due to logarithmic enhancement of the polarization operator (and hence of the corresponding Stoner parameter); we will pursue these phases in this subsection.

To determine which order (SDW or CDW) is promoted by nesting, we appeal to the following patch model [25,26], which is a minimal model to account for interactions on a

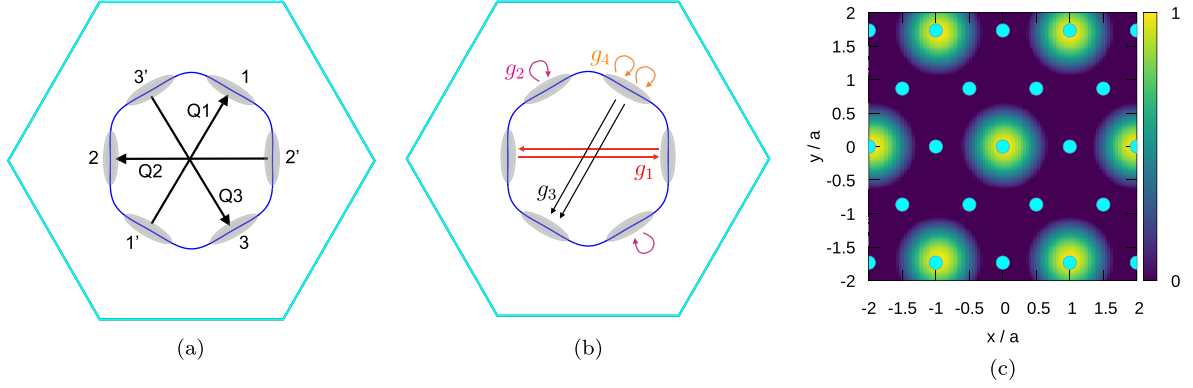


FIG. 9. (a) Nested Fermi surface. Three opposite edges are nested with vectors $\mathbf{Q}_1, \mathbf{Q}_2, \mathbf{Q}_3$. We have chosen to label pairs of patches, i.e., $\{1, 1'\}$, which are connected by a \mathbf{Q}_i vector. (b) The interactions detailed in the patch model (7). (c) The z component of the spin density wave (10), with $\varphi_1 = \varphi_2 = \varphi_3 = (0, 0, 1)$. Light blue circles represent the positions of the TAL sites. The nesting vectors, \mathbf{Q}_i , are determined numerically. The corresponding SDW lattice constant is, from $\mathbf{Q}_i \cdot \mathbf{L}_i = 2\pi$, found to be $|\mathbf{L}_i| \approx 2a$.

nested Fermi surface,

$$\begin{aligned} \mathcal{L}_\alpha^{(0)} &= \frac{1}{2} \sum_{p, \alpha, \sigma} \left[\begin{array}{c} \psi_{\alpha, \sigma, p}^\dagger \\ \psi_{\alpha', \sigma, p}^\dagger \end{array} \right] \\ &\quad \times \begin{bmatrix} i\omega_n - \varepsilon_{\alpha, p} & 0 \\ 0 & i\omega_n + \varepsilon_{\alpha, p} \end{bmatrix} \begin{bmatrix} \psi_{\alpha, \sigma, p} \\ \psi_{\alpha', \sigma, p} \end{bmatrix}, \\ \mathcal{L}_\alpha^{(\text{int})} &= -\frac{1}{2} \sum_{p_i, \alpha \neq \beta, \sigma, \sigma'} \left[g_1 \psi_{\alpha, \sigma, p_1}^\dagger \psi_{\beta, \sigma', p_2}^\dagger \psi_{\alpha, \sigma', p_3} \psi_{\beta, \sigma, p_4} \right. \\ &\quad + g_2 \psi_{\alpha, \sigma, p_1}^\dagger \psi_{\beta, \sigma', p_2}^\dagger \psi_{\beta, \sigma', p_3} \psi_{\alpha, \sigma, p_4} \\ &\quad + g_3 \psi_{\alpha, \sigma, p_1}^\dagger \psi_{\alpha', \sigma', p_2}^\dagger \psi_{\beta, \sigma', p_3} \psi_{\beta, \sigma, p_4} \left. \right] \\ &\quad - \frac{1}{2} \sum_{p_i, \sigma, \sigma'} g_4 \psi_{\alpha, \sigma, p_1}^\dagger \psi_{\alpha', \sigma', p_2}^\dagger \psi_{\alpha, \sigma', p_3} \psi_{\alpha, \sigma, p_4}. \end{aligned} \quad (7)$$

The model $\mathcal{L}_\alpha^{(0)}$ describes the Fermi surface patch α , and its nesting with patch α' [see Fig. 9(a)] with all patches treated as being independent of each other. Here, p represents the momentum of patch α and σ, σ' labels the spin. Our notation in $\mathcal{L}_\alpha^{(0)}$ takes into account the nesting property $\varepsilon_{\alpha', p} = -\varepsilon_{\alpha, p}$.

Interactions between patches are accounted for in the second term of Eq. (7), $\mathcal{L}_\alpha^{(\text{int})}$. Here we account for allowed four-fermion interaction processes both for fermions in different patches and within the same patch. Note that momentum conservation is assumed, $\mathbf{p}_1 + \mathbf{p}_2 = \mathbf{p}_3 + \mathbf{p}_4$ (modulo a reciprocal lattice vector \mathbf{G}_i), within the summation. The couplings g_i correspond to the following processes: g_1 is a patch-exchange interaction; g_2 is a density-density interaction for fermions on different patches; g_3 is pair hopping between patches; g_4 is a density-density interaction for fermions on the same patch. Such interaction processes are represented in Fig. 9(b). The interaction process g_3 only exists for special momentum transfer $2\mathbf{Q}_\alpha = \mathbf{G}_i$. For the doped flat band, Fermi surface nesting occurs with vectors $2\mathbf{Q}_\alpha \neq \mathbf{G}_i$, so we must set $g_3 = 0$ since it does not conserve momentum (modulo \mathbf{G}_i).

We do not consider a nesting driven superconductivity, which in a previous work [25] was found to be promoted by $g_3 \neq 0$. Instead we restrict our analysis to CDW and SDW. To treat them on an equal footing, we take the four

component order parameter Φ_μ , with Φ_0 representing CDW and $\Phi = (\Phi_1, \Phi_2, \Phi_3)$ representing SDW. Using a Hubbard-Stratonovich decoupling of the four-fermion interactions, the action is written as a sum over patches $\mathcal{S} = \sum_{\alpha=1}^3 \mathcal{S}_\alpha$, with

$$\begin{aligned} \mathcal{S}_\alpha &= \sum_{\omega_n} \sum_{p \in \mathcal{D}_\alpha} \left(\begin{array}{c} \psi_{\alpha, p}^\dagger \\ \psi_{\alpha', p}^\dagger \end{array} \right) \\ &\quad \times \begin{pmatrix} i\omega_n - \varepsilon_{\alpha, p} & \Phi_\mu \sigma_\mu \\ \Phi_\mu^* \sigma_\mu & i\omega_n - \varepsilon_{\alpha', p} \end{pmatrix} \begin{pmatrix} \psi_{\alpha, p} \\ \psi_{\alpha', p} \end{pmatrix} \\ &\quad + \frac{1}{g_2 - 2g_1} |\Phi_{0, \alpha}|^2 + \frac{1}{g_2} |\Phi_\alpha|^2. \end{aligned} \quad (8)$$

Here α' is the nested FS patch opposite to α , $\sigma_\mu = (\sigma_0, \sigma)$ are the spin Pauli matrices, and spin indices are suppressed. The momenta are restricted to lay within a patch region, denoted $p \in \mathcal{D}_\alpha$; this also prevents double counting of states. In the following we make use of the nesting property $\varepsilon_{\alpha', p} = -\varepsilon_{\alpha, p}$. The free energy per patch α is obtained by integrating over fermionic fields, and subsequently performing an expansion in bosonic fields Φ_μ , which to quartic order yields

$$\begin{aligned} \mathcal{F}_\alpha &= \left(\frac{1}{g_2 - 2g_1} - a(T) \right) \Phi_0^2 + \left(\frac{1}{g_2} - a(T) \right) \Phi^2 \\ &\quad + b(T) (|\Phi_0|^4 + |\Phi|^4 + |\Phi \times \Phi^*|^2 + 4|\Phi|^2 |\Phi_0|^2 \\ &\quad + \Phi \cdot \Phi (\Phi_0^*)^2 + \Phi^* \cdot \Phi \Phi_0^2). \end{aligned} \quad (9)$$

Here,

$$\begin{aligned} a(T) &= \sum_{\omega_n, p \in \mathcal{D}_\alpha} (\omega_n^2 + \varepsilon_{\alpha, p}^2)^{-1} > 0, \\ b(T) &= \frac{1}{2} \sum_{\omega_n, p \in \mathcal{D}_\alpha} (\omega_n^2 + \varepsilon_{\alpha, p}^2)^{-2} > 0. \end{aligned}$$

To minimize the free energy, the quartic term dictates that the system chooses a purely real vector $\Phi \in \mathbb{R}^3$ and purely imaginary scalar $\Phi_0 \in \mathbb{I}$, or vice versa. Then it is easy to see that for $g_1 > 0$ the SDW order, Φ , is favored, while for $g_1 < 0$ the CDW order, Φ_0 , is favored. Finally, if $g_1 = 0$, the free energy has an $\text{SO}(4)$ symmetry for the order parameter (Φ_0, Φ) ,

and the system may spontaneously choose any angle in the $SO(4)$ order parameter manifold, thereby admixing CDW and SDW. We assume that all interactions are repulsive, implying that $g_1 > 0$ and hence that SDW dominates. Summing over all α , and Fourier transforming (extending momentum summation to $\mathcal{D}_\alpha \rightarrow \infty$), we obtain the following structure for the real-space SDW order parameter,

$$\Phi(\mathbf{r}) = \Phi_1 \cos(\mathbf{Q}_1 \cdot \mathbf{r}) + \Phi_2 \cos(\mathbf{Q}_2 \cdot \mathbf{r}) + \Phi_3 \cos(\mathbf{Q}_3 \cdot \mathbf{r}). \quad (10)$$

Here $\Phi_i \in \mathbb{R}^3$ are constant real vectors with equal magnitude, but arbitrary orientation. Hence this order parameter is highly degenerate. We plot one such realization, $\Phi_1 = \Phi_2 = \Phi_3 = (0, 0, 1)$, in Fig. 9(c).

This order does not fully gap the charge carriers at the Fermi surface, and so would not be straightforward to detect in transport measurements. However, the SDW ordering wave vectors, \mathbf{Q}_i , reconstruct the Fermi surface to form small Fermi pockets; such an effect could be measured via, e.g., Shubnikov–de Haas oscillations.

C. Superconductivity

It is worthwhile to mention the possibility of nesting-induced superconductivity, which follows from the approach developed in Ref. [25]. That work predicts that graphene, doped such that the Fermi surface passes through the M point of the Brillouin zone [Fig. 1(d)], will exhibit superconductivity. The Fermi surface at this point is hexagonal with vertices which touch the M points. Such a Fermi surface exhibits nesting and is also found in the band structure of our artificial lattice when the chemical potential is just above or just below the Dirac cones [see bands 1, 2 and 4, 5 in Fig. 1(b), for example]. In this case the nesting vector is equal to a reciprocal lattice vector ($2\mathbf{Q}_{\alpha\beta} = \mathbf{G}_i$) and hence the coupling, g_3 , is allowed. Inclusion of this coupling dramatically influences the phase diagram, promoting $d + id$ superconductivity as the leading instability [25]. For the band structures we consider in this work [e.g., Fig. 1(b) and Fig. 5(c)] this situation is realized at four different values of E_F , each of which correspond to a van Hove singularity in the density of states. That is once within each of the bands 1, 2, 4, 5 at the energy where those bands reach the M point (midpoint between K and K').

In addition to nesting-induced superconductivity for doping at the M point, there is a recent proposal for *pseudospin*

superconductivity in Dirac-like bands which occurs for doping slightly above or below the K and K' points, which has been worked out for the cases with [27] and without spin-orbit coupling [28,29]. Such situations are directly relevant to hole or electron doping in the artificial TAL system considered here, with chemical potential positioned near either of the two sets of Dirac bands.

VI. CONCLUSIONS

Previously, two-dimensional artificial triangular anti-dot lattices in a semiconductor have attracted attention due to the possibility of studying Dirac and topological physics. In the present work we shift the focus to electron-electron correlation effects. To be specific we concentrate on GaAs and come to the following conclusions.

(i) At a sufficiently strong anti-dot potential modulation, W , the 3rd, 4th, and 5th minibands of the system mimic the dispersion of an emergent kagome lattice. Hence, we map the triangular anti-dot system to an effective Hubbard model on a kagome lattice. The model manifests strong electron-electron correlations.

(ii) We demonstrate the significant practical experimental advantage of holes compared to electrons. Due to the spin-orbit interaction of holes, the strength of the potential modulation, W , necessary to access the strongly correlated regime is 2 to 3 times smaller for holes than for electrons.

(iii) We demonstrate that, at a sufficiently large W and dependent on the value of the chemical potential, the system develops a Mott transition and also several kinds of commensurate charge density waves.

(iv) We also show that, in the regime of not too large W (precursor to strong correlations) and dependent on the value of the chemical potential, the system has a robust ferromagnetic Stoner instability and also superconducting, charge density wave, and spin density wave instabilities.

ACKNOWLEDGMENTS

We wish to acknowledge useful discussions with A. R. Hamilton, J. Ingham, O. Klochan, T. Li, and D. Wang. This research was supported by an Australian Government Research Training Program (RTP) Scholarship. We have also received support from the Australian Research Council Centre of Excellence in Future Low-Energy Electronics Technology (FLEET) (Grant No. CE170100039).

-
- [1] L. Balents, C. R. Dean, D. K. Efetov, and A. F. Young, *Nat. Phys.* **16**, 725 (2020).
- [2] Z. Zhang, Y. Wang, K. Watanabe, T. Taniguchi, K. Ueno, E. Tutuc, and B. J. LeRoy, *Nat. Phys.* **16**, 1093 (2020).
- [3] M. Kang, L. Ye, S. Fang, J.-S. You, A. Levitan, M. Han, J. I. Facio, C. Jozwiak, A. Bostwick, E. Rotenberg *et al.*, *Nat. Mater.* **19**, 163 (2020).
- [4] Y. Cao, V. Fatemi, S. Fang, K. Watanabe, T. Taniguchi, E. Kaxiras, and P. Jarillo-Herrero, *Nature (London)* **556**, 43 (2018).
- [5] Z. Liu, F. Liu, and Y.-S. Wu, *Chin. Phys. B* **23**, 077308 (2014).
- [6] B. R. Ortiz, S. M. L. Teicher, Y. Hu, J. L. Zuo, P. M. Sarte, E. C. Schueller, A. M. M. Abeykoon, M. J. Krogstad, S. Rosenkranz, R. Osborn *et al.*, *Phys. Rev. Lett.* **125**, 247002 (2020).
- [7] C. C. Zhu, X. F. Yang, W. Xia, Q. W. Yin, L. S. Wang, C. C. Zhao, D. Z. Dai, C. P. Tu, B. Q. Song, Z. C. Tao *et al.*, [arXiv:2104.14487](https://arxiv.org/abs/2104.14487).
- [8] K. Y. Chen, N. N. Wang, Q. W. Yin, Y. H. Gu, K. Jiang, Z. J. Tu, C. S. Gong, Y. Uwatoko, J. P. Sun, H. C. Lei *et al.*, *Phys. Rev. Lett.* **126**, 247001 (2021).
- [9] B. R. Ortiz, P. M. Sarte, E. M. Kenney, M. J. Graf, S. M. L. Teicher, R. Seshadri, and S. D. Wilson, *Phys. Rev. Mater.* **5**, 034801 (2021).

- [10] S. Ni, S. Ma, Y. Zhang, J. Yuan, H. Yang, Z. Lu, N. Wang, J. Sun, Z. Zhao, D. Li *et al.*, *Chin. Phys. Lett.* **38**, 057403 (2021).
- [11] Y.-X. Jiang, J.-X. Yin, M. M. Denner, N. Shumiya, B. R. Ortiz, G. Xu, Z. Guguchia, J. He, M. S. Hossain, X. Liu *et al.*, *Nat. Mater.* **20**, 1353 (2021).
- [12] O. A. Tkachenko, V. A. Tkachenko, I. S. Terekhov, and O. P. Sushkov, *2D Mater.* **2**, 014010 (2015).
- [13] J. Pedersen, C. Flindt, N. Asger Mortensen, and A.-P. Jauho, *Phys. Rev. B* **77**, 045325 (2008).
- [14] C. Flindt, N. A. Mortensen, and A.-P. Jauho, *Nano Lett.* **5**, 2515 (2005).
- [15] D. Q. Wang, Z. E. Krix, O. P. Sushkov, I. Farrer, D. A. Ritchie, A. R. Hamilton, and O. Klochan (unpublished).
- [16] L. Du, Z. Liu, S. J. Wind, V. Pellegrini, K. W. West, S. Fallahi, L. N. Pfeiffer, M. J. Manfra, and A. Pinczuk, *Phys. Rev. Lett.* **126**, 106402 (2021).
- [17] J. M. Luttinger, *Phys. Rev.* **102**, 1030 (1956).
- [18] D. S. Miserev and O. P. Sushkov, *Phys. Rev. B* **95**, 085431 (2017).
- [19] L. Landau and E. Lifshitz, *Quantum Mechanics*, 3rd ed. (Pergamon, Oxford, 1977), pp. 197–224.
- [20] R. Winkler, *Spin-Orbit Coupling Effects in Two-Dimensional Electron and Hole Systems*, Springer Tracts in Modern Physics (Springer, Berlin, 2003).
- [21] O. P. Sushkov and A. H. Castro Neto, *Phys. Rev. Lett.* **110**, 186601 (2013).
- [22] H. D. Scammell and O. P. Sushkov, *Phys. Rev. B* **99**, 085419 (2019).
- [23] D. I. Khomskii, *Instabilities and Phase Transitions in Electronic Systems* (Cambridge University Press, Cambridge, 2010), pp. 188–228.
- [24] H. Matsuoka, S. E. Barnes, J. Ieda, S. Maekawa, M. S. Bahramy, B. K. Saika, Y. Takeda, H. Wadati, Y. Wang, S. Yoshida *et al.*, *Nano Lett.* **21**, 1807 (2021).
- [25] R. Nandkishore, L. S. Levitov, and A. V. Chubukov, *Nat. Phys.* **8**, 158 (2012).
- [26] S. Maiti and A. V. Chubukov, in *Lectures on the Physics of Strongly Correlated Systems XVII: Seventeenth Training Course in the Physics of Strongly Correlated Systems*, edited by A. Avella and F. Mancini, AIP Conf. Proc. No. 1550 (AIP, New York, 2013), p. 3.
- [27] H. D. Scammell, J. Ingham, M. Geier, and T. Li, [arXiv:2111.07252](https://arxiv.org/abs/2111.07252).
- [28] T. Li, J. Ingham, and H. D. Scammell, *Phys. Rev. Res.* **2**, 043155 (2020).
- [29] T. Li, M. Geier, J. Ingham, and H. D. Scammell, *2D Mater.* **9**, 015031 (2022).